

Atomic scale strain engineering of layered sheets on the surfaces of two-dimensional materials

N. Sarkar¹, R.C. Dynes^{2,3}, P.R. Bandaru^{2,3,4}

¹Department of Mechanical Engineering, ²Department of Physics,

³Program in Materials Science,

University of California, San Diego, La Jolla, CA 92093-0411

Abstract: The modulation of the atom spacings in the sheets of two-dimensional (2D) materials offers a modality for the tuning of related physical and chemical attributes of materials. In this context, we present a methodology, deploying zero-dimensional tip induced forces, for the modification of the mechanical and electrical attributes of strained graphitic sheets, single layer graphene, and niobium diselenide (NbSe_2). *In situ* topographic and spectroscopic probing through electrical current tunneling was utilized to monitor the modification. A distinct response of the elastic deformation attributes between 2D-like sheets of graphene and NbSe_2 was indicated and attributed to local bonding configuration. Further, the deformation of the formed Moiré patterns, as a function of the 2D sheet stacking configurations, was probed for the related van der Waals (vdW) bonding strength. The influence of the grain interiors as well as the grain boundaries and domain walls together with the influence on the electronic band structure is noted. The related study also resolves a decades-long debate on anomalously high atomic amplitudes measured on graphitic surfaces.

Main: The emergent fields of twistronics [1] and straintronics [2] hinges on the application of the understanding of atomic scale deformation mechanisms for micro- and macro-scale utilization. The manifestation of unique properties from using the related strain as a degree of freedom has brought forth unexpected characteristics in 2D materials, e.g., superconductivity [3] and ferromagnetism [4] in bilayer graphene and chalcogenides through hetero-strain [5-9], hydrostatic pressure [10], or substrate engineering [11]. Yet another method to induce measurable strain involves the controlled deformation of atomic bonds through electrical tunneling induced forces [12-14]. The type and magnitude of the strain in 2D systems would be expected to be a function of the local atomic configuration as well as the interaction, and involve both covalent and vdW bonding, the relative extents of which would be based

on the composition and related structural anisotropy. The ease of exfoliation of the native bulk materials, to yield 2D sheets, and constituted heterostructures [15] would also be dependent on such issues and need to be investigated for technological implications.

We suggest that scanning tunneling microscopy (STM) and related spectroscopy can yield significant insights into such strain-based effects. For instance, a large (/small) tip-sample gap as monitored through a small (/large) tunneling current is expected to induce small (/large) deformation of the 2D layer: **Fig. 1(a)**. However, previous STM studies on 2D material-based surfaces has not clearly elucidated the bonding influences due to the conflation of various electronic and mechanical tip-sample interactions [16-18], mediated through surface forces [19-21]. Here, we present experiments and related analyses of two prototype 2D materials, *i.e.*, through graphitic sheets and NbSe_2 , with the attribute of one- and two-atom based systems, respectively. Moreover, highly oriented pyrolytic graphite (HOPG) has been extensively used in STM related work as a calibration standard [22-24] for height determination over the *steps* arising from a presumed atomic flatness and surface cleanliness [25-27]. The observed steps, *e.g.*, **Fig. 1(b)**, are presumed to arise from a difference in the elevation of graphene sheets on either side and would be distinguished ideally by multiples of 3.4\AA , corresponding to the layer-by-layer spacing of the sheets. However, previous STM measurements have indicated some confusion on the deduced step heights, arising from the possible lack of flatness of the graphene sheet. Such an attribute may arise from atomic corrugation yielding an enhancement of the measured amplitudes [12-14]. For instance, while the measured atomic amplitudes on graphite surface are expected to be 0.2\AA from Local Density of States (LDOS) calculations [28-31], abnormally high atomic amplitudes, of the order of up to 24\AA were indicated [12-14]. Such anomalies have been attributed to the tip-surface interactions which may induce local elastic deformation of graphite surfaces particularly at small distances [12,32]. While the oscillations follow the modeled LDOS based contours [31], extant models[28-31] of tip-sample interaction involving localized elastic deformation – based on a particular interatomic potential interaction model[12,14,29,33-36] involving variable tip geometry, are inadequate to quantitatively account for the large magnitude.

In our own observations using the same tip over a range of measurements, we have seen such enhanced amplitudes on sheets of graphite, but nevertheless the difference of the mean of the corrugations across the step has yet been constant over a range of tunneling conditions. Consequently, the step height-based standard in graphite samples is reconfirmed as an accurate height calibration feature in the STM. It was also noted that while the spatial frequency of the oscillations was $\sim 2.5\text{\AA}$, corresponding to the C atom – C atom spacing shown in the *inset*, there is yet the issue of the unexpectedly large atomic corrugations on graphitic surfaces - previously attributed, somewhat tentatively [12], to tip-induced surface deformation. The observed surface variation [32] should be

nominally reflected in the sliding or the shear between the basal planes in 2-D layered materials and would be materials specific. To glean further insight, we compared the atomic topography of single-layer graphene (SLG) - as well as across the steps formed by exfoliating graphite in Fig.1(d) and NbSe₂ in Fig. 1(e). While oscillations were again observed: **Fig. 1(e)**, with a spatial frequency of ~ 3.4 Å, corresponding to the van der Waals spacing [37] they are less pronounced compared to those in graphite. The step height was constant at ~ 12.5 Å, as related to the height of the Se-Nb-Se sheet, concordant to NbSe₂[37] . Comparing the magnitude of the oscillations, it may be considered that the graphite surface is more pliable compared to surfaces of NbSe₂ and SLG.

The atomic topography, related to the corrugations, also yields a rationale for the indicated placement of the atoms, as further indicated in **Fig. S1** of the *Supplementary Information 1*. Through comparing the topography at two different tip-sample distances, *i.e.*, closer (/further) spacing at larger (/smaller) currents corresponding to larger (/smaller) atomic corrugation amplitudes is indicated. There then arises a rationale, from elastic theory [12], for the higher corrugations through tip induced local deformation at an atom – either outwards (/inwards) related to attractive (/repulsive) tip-sample interactions and yields a guide for the indicated placement of the atoms, *i.e.*, the hills (/valleys) corresponding to outward (/inward) atomic deformations. It has been suggested [12] that the inward (/outward) atomic deformation would be opposed by a stronger (/weaker) restoring repulsive force, and the related difference was observed [12] in terms of a preference towards stronger minima in the atomic topography of graphite: see *Supplementary Information 2*.

The measured atomic amplitudes of graphitic surfaces, NbSe₂ and SLG and their average is compared as a function of I_{tip} (at a constant V_{sample}): **Fig. 2(a)**, and V_{sample} (at a constant I_{tip}): **Fig. 2(b)**. With an increase in the I_{tip} from 10 nA to 90 nA or equivalently a decrease in V_{sample} from 500 mV to 50 mV, we observe an anomalous increase in the atomic amplitudes in graphite from ~ 1.5 Å to ~ 3.5 Å (as also observed in [12-14]) while the amplitude at the step is relatively constant at around 3 Å. In contrast, a smaller enhancement was seen in NbSe₂ of the atomic amplitudes – in the range of 1.5 Å to 2.5 Å and SLG – in the range of 2 Å to 2.5 Å: **Fig. 2**. A reduction in tip-sample gap leads to a diminution in tunneling gap resistance: R_{gap} (defined as the V_{sample} / I_{tip}) - also see **Fig. S2** in *Supplementary Information 3*. A similar tip-surface interaction with the topmost layer of graphite as well as the SLG is nominally expected yielding comparable deformation. However, the SLG placed on an atomically smooth (**ref. Fig. 2**) mica substrate, shows much lower atomic amplitude. The vdW bonding between the layers in graphite distinct from a stronger bonding of the SLG to the mica [38,39] seems to be involved. Indeed, the extent of deformation is seen to be similar for NbSe₂ and SLG, suggesting a similar bonding mechanism of the top sheet with respect to the underlying bulk/substrate. It is then suggested that the SLG-mica adhesion may be comparable in magnitude to that in the Se-Nb-Se

trilayers. Consequently, tip-sample mediated deformation is suggested as a possible methodology for monitoring surface-bulk interactions.

It has been suggested [12,32] that the attractive (/compressive) forces from the tip cause an outward (/inward) deformation of the surface which would be manifested through elastic shear along the basal planes: **Figs. 3(a)** and **3(b)**, respectively. The magnitude of the shear would be dependent on the layer-to-layer spacing. Assigning one atom to one layer, we see that the graphite sheets would be one-layer thick at $\sim 3.2 \text{ \AA}$ while a NbSe_2 surface sheet would be three-atoms (/layers) thick at $\sim 12.5 \text{ \AA}$. If it is hypothesized that the extent of shear is larger for a *heavier* multilayered sheet compared to a *thinner* single layer sheet, then the extent of deformation and atomic amplitudes would be smaller (/larger) in NbSe_2 (/graphite), given similar tip-induced forces.

As indicated earlier, the atomic constitution as well as the structural anisotropy determine the extent of layer deformation and observed atomic amplitudes. Such an aspect is also manifest in the examined *tearing* pattern observed after exfoliation. In the case of graphite, a *serrated* step feature was seen, *e.g.*, in **Fig. 3(e)** whereas the NbSe_2 step terraces are fractured by 100\AA : **Fig. 3(f)** inset. The triangular edges in the graphite follow the **a** and **b** crystal axes - indicated by red and blue arrows, respectively in **Fig. 3(e)**, with respect to the step edge/exfoliation direction (labeled by a white arrow). The exfoliation is more closely aligned to **b** implying more bond breaking in that direction. Alternatively, in NbSe_2 , there is a propensity for one-sheet (of triatomic-layer) deep pitting at both the micron and nanometer scales.

In surface deformation of 2D material-based sheets, the outstanding features are related to the constitution of the sheet, *i.e.*, number of layers and atomic makeup, as well as the nature of the bonding of the topmost surface layer to the near surface layers. Such behavior is in contrast to what would be nominally expected in a standard constant current STM mode [40-42], where the tip traces the potential contours over the rigid atomic surface without deforming it. It would then be of interest to investigate the deformation mechanisms related to layers slightly out of registry with respect to each other. Such an aspect has recently found much favor through the study of Moiré patterns, with spatially variable inter-layer bonding [25,43-45]. Considering the graphene layer as constituted from C atoms placed at two distinct lattice sites: A and B, the layers in graphite may either be placed such that: (i) the A and B atoms are directly on top of each other, *i.e.*, the AA or BB type stacking, or (ii) the atoms of the A (/B) lattice site in one layer sit atop the B (/A) atoms of the layer beneath, *i.e.*, the AB or BA stacking. It is well known that the latter A-B/B-A based Bernal stacking is favored from an energetic stability point of view [43-45]. However, when twisting one layer with respect to the other, both types of stacking, resulting in AA as well as AB type domains, would emerge and contribute to the observed Moiré. Such a pattern of domains could arise, for instance, from a twist of a top monatomic layer with respect to the

underlying layer/substrate, with the pattern periodicity directly related to the extent of misregistration. The twistronics implication of such orientability has been manifested in various structural, electronic, and physico-chemical attributes [46-50],

We demonstrate that the tip-induced deformation across the Moiré pattern reveals local vdW bonding variability [46-48] as well as interlayer interactions [43-45]. An instance of a pattern formed by a 4.2° twist angle in the upper layers of graphite is indicated in **Fig. 4(a)**. Both AA as well as AB type domains are observed and the lines connecting the AA region are termed domain walls (DWs) and cross over the AB/BA domains. Such DWs are of much interest due to specific topological characteristics [49], favorable for soliton propagation [48], etc. Scanning the tip in various directions, e.g., AA \rightarrow AA \rightarrow AA, along the DW: [blue dotted line](#), and AB \rightarrow AA \rightarrow AB: [red dotted line](#), in **Fig. 4(c)** and **Fig. 4(e)** respectively, yields high (low) atomic amplitude in the AA (AB) domains, and may be ascribed to the related weak (strong) vdW-related bonding. The surface contouring related to the Moiré, and due to the specific stacking configuration, may then be monitored through the I_{tip} : **Fig. 5(d)**. Considering the AA \rightarrow AB \rightarrow AA trajectory: **Fig. 4(e)**, the DW bonding is seen to be intermediate to the two modes of stacking.

The deformation amplitudes of the domains as estimated from **Figs. 4(c)** and **4(e)** are indicated in **Fig. 5(a)** - as a function of the I_{tip} and R_{gap} . At a reduced tip-sample distance, there is considerable outward deformation/*bulging* out of the AA regions by $\sim 11\text{\AA}$ owing to unstable stacking whereas the AB regions are much less deformed, i.e., at $\sim 3\text{\AA}$ given the presumed stable stacking configurations [43-45]. The DW response is intermediate, as also previously indicated. The extent of observed deformation is then a gauge of the relative bonding strength and marks the localized topography of the Moiré pattern.

The differential conductance (dl/dV) – as related to the local DOS, measured by probing a Moiré pattern, formed at a lower twist angle (of $\sim 0.8^\circ$) is shown in **Fig. 5(b)**. Such low angle twists have been associated [51] with the occurrence of van Hove singularities (vHs) [52] which converge into a single peak, representing a high DOS flat band on deformation: Fig. 6(b) bottom to top inset. A flat band attribute indicates minimal energy dispersion. Spectroscopy on the AA domains at different tip-sample gaps reveals the onset of such flat band formation, as deduced from the reduced full width half maxima (FWHM) of the associated conductance peaks, with decreasing R_{gap} . Also see *Supplementary Information 4*, for further discussion on Moiré patterns as well as the interpretation of the measurements. It is then indicated that the deformed top layer has not electronically decoupled from the underlying layer and mimics the deformation indicated in **Fig. 3(b)** rather than the one in **Fig. 4(d)**.

Our work has demonstrated the interplay between inter-layer coupling as well as the association with the substrate of exemplar one-atom and two-atom constituted 2D material systems, in response to electromechanical forces at the nanoscale. This was achieved through an analysis of the atomic scale

corrugations and ascribed to the modulation of the related physico-chemical bonding attribute. The aspect that band structure tuning would be feasible through the controlled surface deformation would be of importance in the *in situ* tuning and probing of materials properties.

Methods:

Materials, Exfoliation and Layer synthesis

Highly oriented pyrolytic graphite (HoPG) and niobium diselenide (NbSe_2) were freshly cleaved from crystals before loading. The choice of HoPG with roughly micron sized grains (ZYH grade from Advanced Ceramics) favors a dense occurrence of step heights as well as multiple moirés patterns of different twist angles. Single crystals of 2H- NbSe_2 millimeter grain sizes were grown by chemical vapor deposition at AT&T Bell labs. Single layer graphene was grown by chemical vapor deposition (CVD) of methane precursor on copper foil and then polymer-assisted wet transfer of graphene was done onto cleaved mica substrates. After dissolving the polymer and thermally evaporating Ti/Au contacts, the graphene/mica stack was baked in an oven at 250°C for a week to dehydrate and degas before loading into the STM.

Electrical Measurements

All imaging was done using a custom-built tunneling microscope with a RHK controller at room temperature and atmospheric pressure. All topography measurements have been performed in standard constant current mode at ~ 0.5 Hz scanning frequency using a mechanically snipped Pt/Ir tip. The spectroscopy measurements utilized a lock in modulation of 3mV at 5kHz.

Calibration and Data analysis

Topographic heights of all images were calibrated using the constant step height measured on graphite and NbSe_2 monatomic steps that remains constant irrespective of tunneling conditions. The same tip was used to measure the average atomic heights of graphite, NbSe_2 and SLG. Step heights are measured by the difference in mean of the two waveforms on either side of the step. Atomic heights of all materials are averaged over 20 peak-to-peak amplitudes. The conductance peak amplitudes in Fig. 6b have been normalized to show the change in its FWHM (or, flat band tuning) as a function of deformation only.

References

1. Wu, D., Pan, Y., & Min, T. Twistrionics in graphene, from transfer assembly to epitaxy. *Applied Sciences* **10**, 4690 (2020).
2. Guinea, F., Katsnelson, M. & Geim, A. Energy gaps and a zero-field quantum Hall effect in graphene by strain engineering. *Nature Phys* **6**, 30–33 (2010).
3. Cao, Y., Fatemi, V., Fang, S. et al. Unconventional superconductivity in magic-angle graphene superlattices. *Nature* **556**, 43–50 (2018).
4. Sharpe, A. L. et al. Emergent ferromagnetism near three-quarters filling in twisted bilayer graphene. *Science* **365**, 605–608 (2019).
5. Yasuda, Kenji, et al. Stacking-engineered ferroelectricity in bilayer boron nitride. *Science* **372**, 1458-1462 (2021).
6. Qiao, J.-B., Yin, L.-J. & He, L. Twisted graphene bilayer around the first magic angle engineered by heterostrain. *Phys. Rev. B* **98**, 235402 (2018).
7. Huder, L. et al. Electronic spectrum of twisted graphene layers under heterostrain. *Phys. Rev. Lett.* **120**, 156405 (2018).
8. Zhang, C. et al. Strain distributions and their influence on electronic structures of WSe₂–MoS₂ laterally strained heterojunctions. *Nat. Nanotechnol.* **13**, 152–158 (2018).
9. Jie, Wenjing, et al. Observation of room-temperature magnetoresistance in monolayer MoS₂ by ferromagnetic gating. *ACS nano.* **11**, 6950-6958 (2017).
10. Snider, Elliot, et al. Room-temperature superconductivity in a carbonaceous sulfur hydride. *Nature* **586**, 373-377 (2020).
11. Yang, S., Chen, Y., & Jiang, C. Strain engineering of two-dimensional materials: Methods, properties, and applications. *InfoMat.* **3**, 397-420 (2021).
12. Soler, J. M., et al. Interatomic forces in scanning tunneling microscopy: giant corrugations of the graphite surface. *Physical review letters* **57**,444 (1986)
13. Binnig, Gerd, et al. Energy-dependent state-density corrugation of a graphite surface as seen by scanning tunneling microscopy. *Europhysics Letters* **1**, 31 (1986).
14. Mamin, H. Jonathon, et al. Contamination-mediated deformation of graphite by the scanning tunneling microscope. *Physical Review B* **34**,9015 (1986).
15. Hu, Zhen, Zhi-Bo Liu, and Jian-Guo Tian. Stacking of exfoliated two-dimensional materials: a review. *Chinese Journal of Chemistry* **38**,981-995 (2020).
16. Miao, Feng, Shi-Jun Liang, and Bin Cheng. Straintronics with van der Waals materials. *npj Quantum Materials* **6**,1-4 (2021).

17. Mooser, E. Physics and chemistry of materials with layered structures. Vols. I-5 (Reidel, Boston) (1976).
18. Park, Jeong Y., et al. Sensing current and forces with SPM. *Materials today*. **13**, 38-45 (2010).
19. Dürig, U., J. K. Gimzewski, and D. W. Pohl. Experimental observation of forces acting during scanning tunneling microscopy. *Physical review letters* **57**, 2403 (1986).
20. Park, Jeong Young, et al. Direct measurement of forces during scanning tunneling microscopy imaging of silicon pn junctions. *Applied Physics Letters* **86**, 172105 (2005).
21. Mate, C. Mathew, et al. Direct measurement of forces during scanning tunneling microscope imaging of graphite. *Surface science* **208**, 473-486 (1989).
22. Tatar, R. C., and S. Rabii. Electronic properties of graphite: A unified theoretical study. *Physical Review B* **25**, 4126 (1982).
23. Batra, Inder P., et al. A study of graphite surface with STM and electronic structure calculations. *Surface Science* **181**, 126-138 (1987).
24. Mándi, Gábor, Gilberto Teobaldi, and Krisztián Palotás. Contrast stability and 'stripe' formation in scanning tunnelling microscopy imaging of highly oriented pyrolytic graphite: the role of STM-tip orientations. *Journal of Physics: Condensed Matter* **26**, 485007 (2014).
25. Wong, H. S., Durkan, C., & Chandrasekhar, N. Tailoring the local interaction between graphene layers in graphite at the atomic scale and above using scanning tunneling microscopy. *ACS nano*. **3**, 3455-3462 (2009).
26. Meyer, Jannik C., et al. On the roughness of single-and bi-layer graphene membranes. *Solid State Communications* **143**, 101-109 (2007).
27. Colton, R. J. et al. *Journal of Vacuum Science and Technology A* **6**, 349-353 (1988).
28. Tersoff, J. Anomalous corrugations in scanning tunneling microscopy: imaging of individual states. *Phys. Rev. Lett.* **57**, 440 (1986).
29. Tersoff, Jerry, and Donald R. Hamann. Theory of the scanning tunneling microscope. *Physical Review B* **31**, 805 (1985).
30. Selloni, Annabella, et al. Voltage-dependent scanning-tunneling microscopy of a crystal surface: Graphite. *Phys. Rev. B* **31**, 2602 (1985).
31. Tekman, E., and S. Ciraci. Atomic theory of scanning tunneling microscopy. *Physical Review B* **40**, 10286 (1989).
32. Pethica, J. B. Comment on "Interatomic forces in scanning tunneling microscopy: Giant corrugations of the graphite surface" *Physical review letters* **57**, 3235 (1986).
33. Tang, S. L., Bokor, J., & Storz, R. H. Direct force measurement in scanning tunneling microscopy. *Applied physics letters* **52**, 188-190 (1988).

34. Smith, D. P. E., G. Binnig, and C. F. Quate. Atomic point-contact imaging. *Applied physics letters* **49**, 1166-1168 (1986).
35. Ciraci, S., and Inder P. Batra. Scanning-tunneling microscopy at small tip-to-surface distances. *Physical Review B* **36**, 6194 (1987).
36. Olsen, Martin, Magnus Hummelgård, and Håkan Olin. Surface modifications by field induced diffusion. *PLoS One* **7**, e30106 (2012).
37. Marezio, M., et al. The crystal structure of NbSe₂ at 15 K. *Journal of Solid State Chemistry* **4**, 425-429 (1972).
38. Shim, Jihye, et al. Water-gated charge doping of graphene induced by mica substrates. *Nano letters* **12**, 648-654 (2012).
39. Bampoulis, Pantelis, et al. Graphene visualizes the ion distribution on air-cleaved mica. *Scientific reports* **7**, 1-8 (2017).
40. Binnig, Gerd, and Heinrich Rohrer. Scanning tunneling microscopy. *Surface science* **126**, 236-2441 (1983).
41. A. Burshtein, S. Lundquist. Tunneling phenomena in solid bodies. *Mir*, (1973).
42. E. Wolf. Electron tunneling spectroscopy principles. Kiev: "Naukova Dumka", **454** (1990)
43. Gong, Lei, et al. Reversible loss of bernal stacking during the deformation of few-layer graphene in nanocomposites. *Acs Nano* **7**, 7287-7294 (2013).
44. Koshino, Mikito, and Edward McCann. Multilayer graphenes with mixed stacking structure: Interplay of Bernal and rhombohedral stacking. *Physical Review B* **87**, 045420 (2013).
45. Latychevskaia, Tataiana, et al. Stacking transition in rhombohedral graphite. *Frontiers of Physics* **14**, 1-7 (2019).
46. Bistritzer, R., & MacDonald, A. H. Moiré bands in twisted double-layer graphene. *Proceedings of the National Academy of Sciences* **108**, 12233-12237 (2011).
47. Song, H. Q., Liu, Z., & Zhang, D. B. Interlayer vibration of twisted bilayer graphene: A first-principles study. *Physics Letters A*, **383**, 2628-2632 (2019).
48. Alden, Jonathan S., et al. Strain solitons and topological defects in bilayer graphene. *Proceedings of the National Academy of Sciences* **110**, 11256-11260 (2013).
49. Huang, Shengqiang, et al. Topologically protected helical states in minimally twisted bilayer graphene. *Physical review letters* **121**, 037702 (2018).
50. McGilly, Leo J., et al. Visualization of moiré superlattices. *Nature Nanotechnology* **15**, 580-584 (2020).
51. Liu, Xiaomeng, et al. Spectroscopy of a tunable moiré system with a correlated and topological flat band. *Nature communications* **12**, 1-7(2021).

52. Kerelsky, Alexander, et al. Maximized electron interactions at the magic angle in twisted bilayer graphene. *Nature* **572**, 95-100 (2019).

[Acknowledgements:](#)

This work was supported as part of the Air Force Grant, an Energy Frontier Research Center funded by the U.S. Department of Energy, Office of Science, Basic Energy Sciences under Award No. DE-SC0019273. The authors wish to thank Michael Rezin for the technical assistance; Hidenori Yamada and Uday Sravan Goteti for suggestive discussions.

[Author contributions:](#)

N. Sarkar did the experimental work and along with P.R. Bandaru wrote the paper. All analysis and discussion were under the supervision of R.C. Dynes and P.R. Bandaru.

[Data availability:](#)

The experimental data and its analysis in the paper and/or in the supplementary information is sufficient to support our conclusions. Additional data can be made available on request.

[Competing interests:](#)

The authors declare no competing interests.

Figures

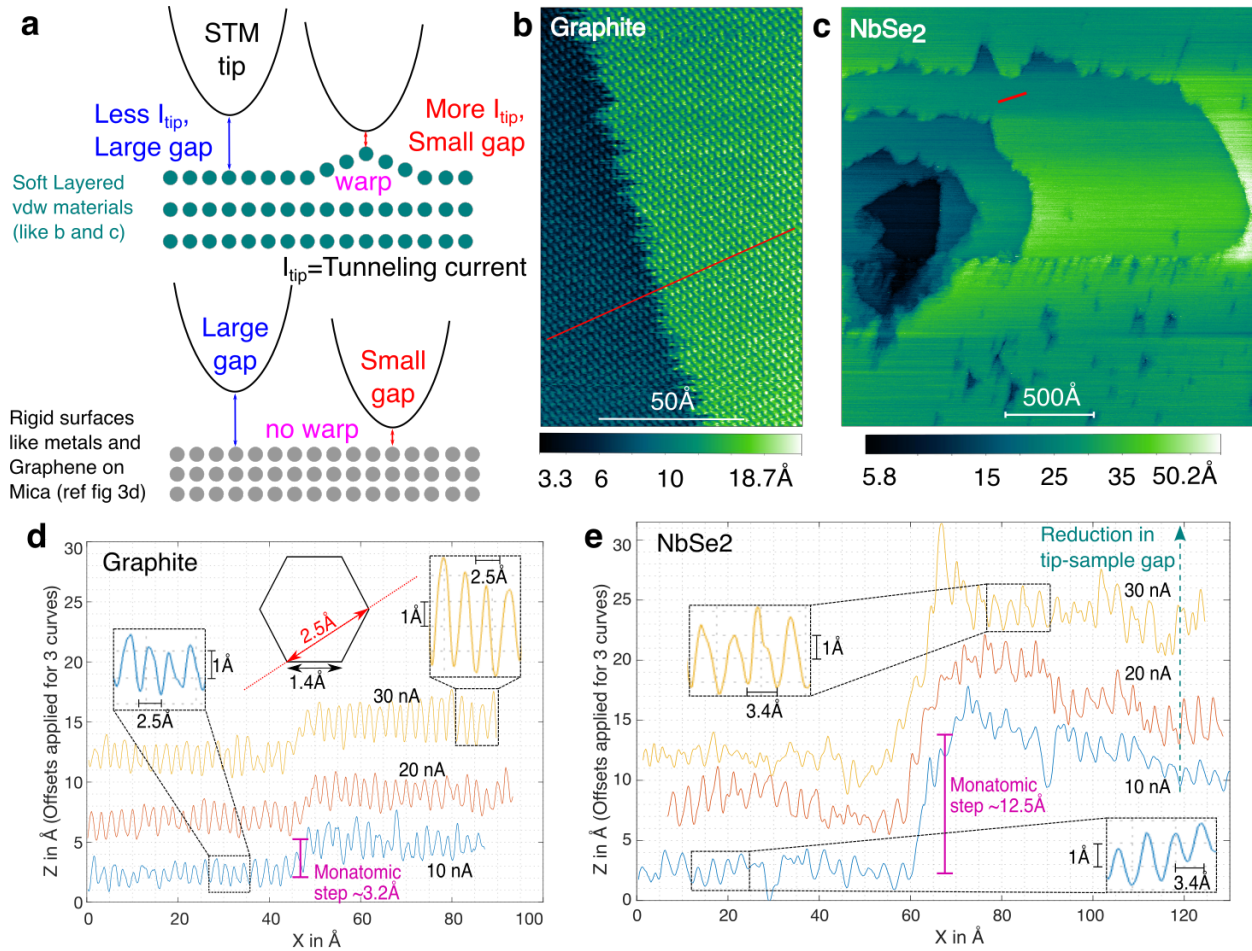


Figure 1: Tip-induced atomic deformation of graphite and NbSe₂ surfaces. **(a)** The expected response of *rigid* vs. *soft* materials to tip induced deformations at large (/small) tip-sample gaps monitored by higher (/small) tunneling currents in scanning tunneling microscopy (STM). The topographic images along steps on **(b)** graphite surface (100Å x 145Å) and **(c)** NbSe₂ surface (2300Å x 2300Å) - at 30nA tunneling current (I_{tip}) and 100mV sample bias (V_{sample}). The color bar at the bottom indicates the measured height in angstroms (Å). The atomic corrugations across the step, as a function of I_{tip} topography along the red line in **(b)** and **(c)** for **(d)** graphite, and **(e)** NbSe₂. The oscillations correspond to corrugations from scanning across individual atoms. The insets show in a magnified view the increase in average oscillation amplitude from 1.5Å to 2.7Å for graphite in **(d)** and from 1.7Å to 2.4Å for NbSe₂ in **(e)**. The spatial frequency on either side of the step remains constant at 2.5Å for graphite - corresponding to the shown atomic spacing in the a-b plane in the middle inset in **(d)** and at 3.4Å for NbSe₂ in **(e)**. The oscillation amplitudes and step heights calculated from **(d)** and **(e)** are plotted in figure 2 as a function of I_{tip} and V_{sample} .

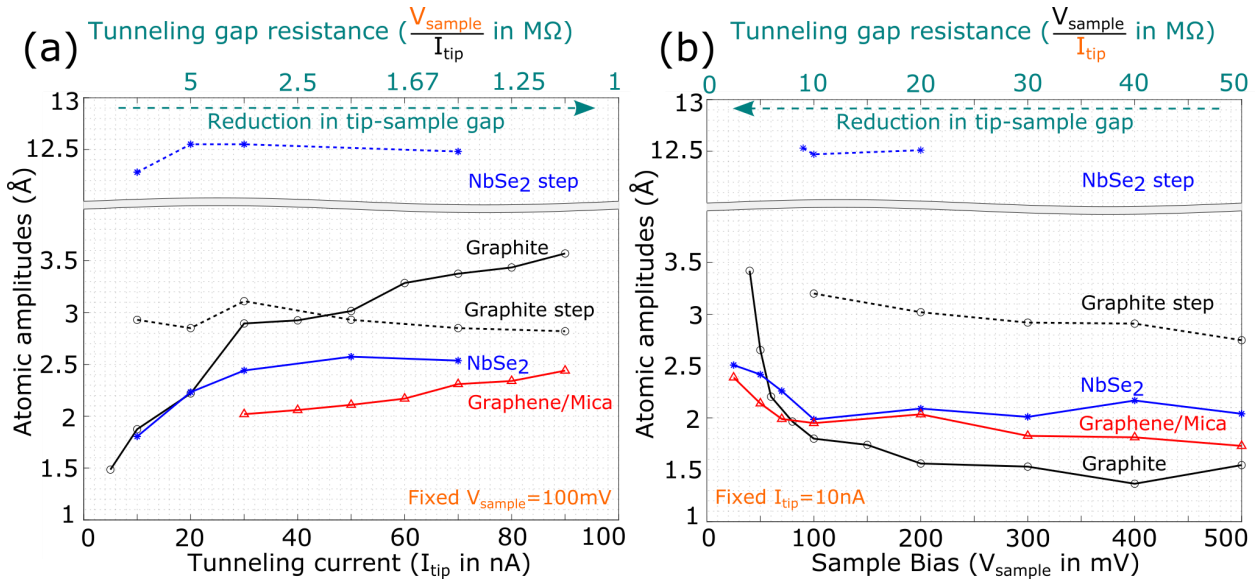


Figure 2. The atomic corrugation amplitude as a function of scanning tip – surface spacing. An increase in the **(a)** tunneling current: I_{tip} , or equivalently a decrease in **(b)** voltage applied to the sample 2D material: V_{sample} , is related to a reduced spacing, and yields higher amplitude of atomic oscillation. A larger increase is found on the graphite surface compared to NbSe₂ and monolayer graphene. The tunneling gap resistance (defined through the ratio of $V_{\text{sample}}/I_{\text{tip}}$) – on the top horizontal axis, reduces with a decreased tip-surface spacing.

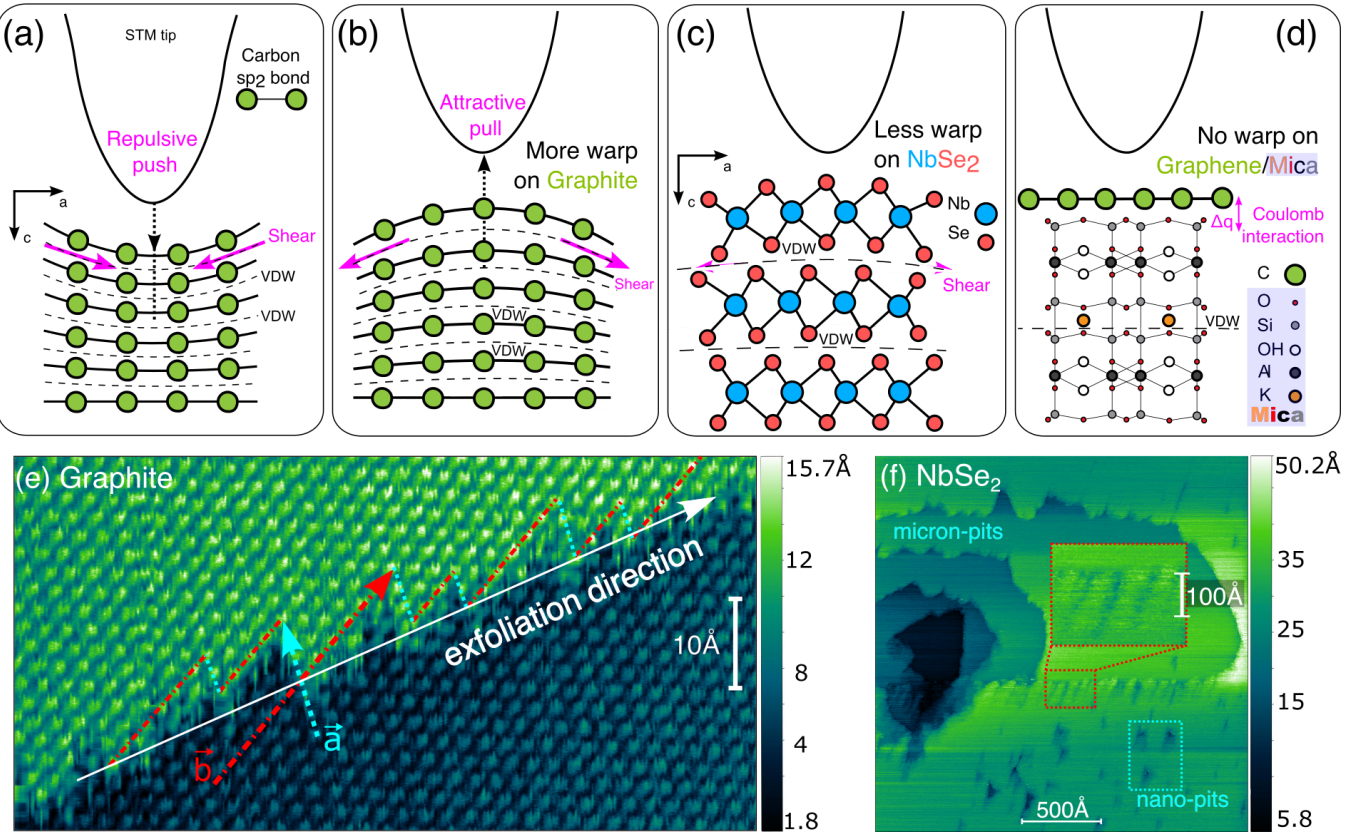


Figure 3: Elastic and plastic deformation in sheets of layered materials. Tip-induced, elastic, local (a) compression, and (b) expansion of graphite surface corresponding to repulsive and attractive interactions, respectively. The related reaction from the underlying near-surface layers is depicted as a shear between the basal planes. Deformations are opposed by shear forces (arrows) along basal planes. In contrast to the representative one-layer surface of graphite the (c) NbSe₂ sheet is composed from three atomic sheets corresponding to Se-Nb-Se. The stronger bonding in the case of the NbSe₂ sheets is comparable to that observed for (d) the single layer graphene (SLG) on a mica substrate, as deduced from the similar atomic corrugation amplitudes, *cf.*, Fig. 2 in both cases, and is manifested in a much smaller warp compared to the case of graphite – where there is substantial bowing and enhanced amplitude. Exfoliation of 2D sheets results in bond breaking and extensive localized plastic deformation and is manifested as a (e) serrated pattern in the atomically resolved topography of graphite, near a step edge. The tearing occurs along the *a* and *b* crystal axes and creates a sawtooth-like pattern. Alternately, a series of monatomic step heights are observed on exfoliated (f) NbSe₂ surfaces, with V-shaped pitting at the micron- and nanometer scales.

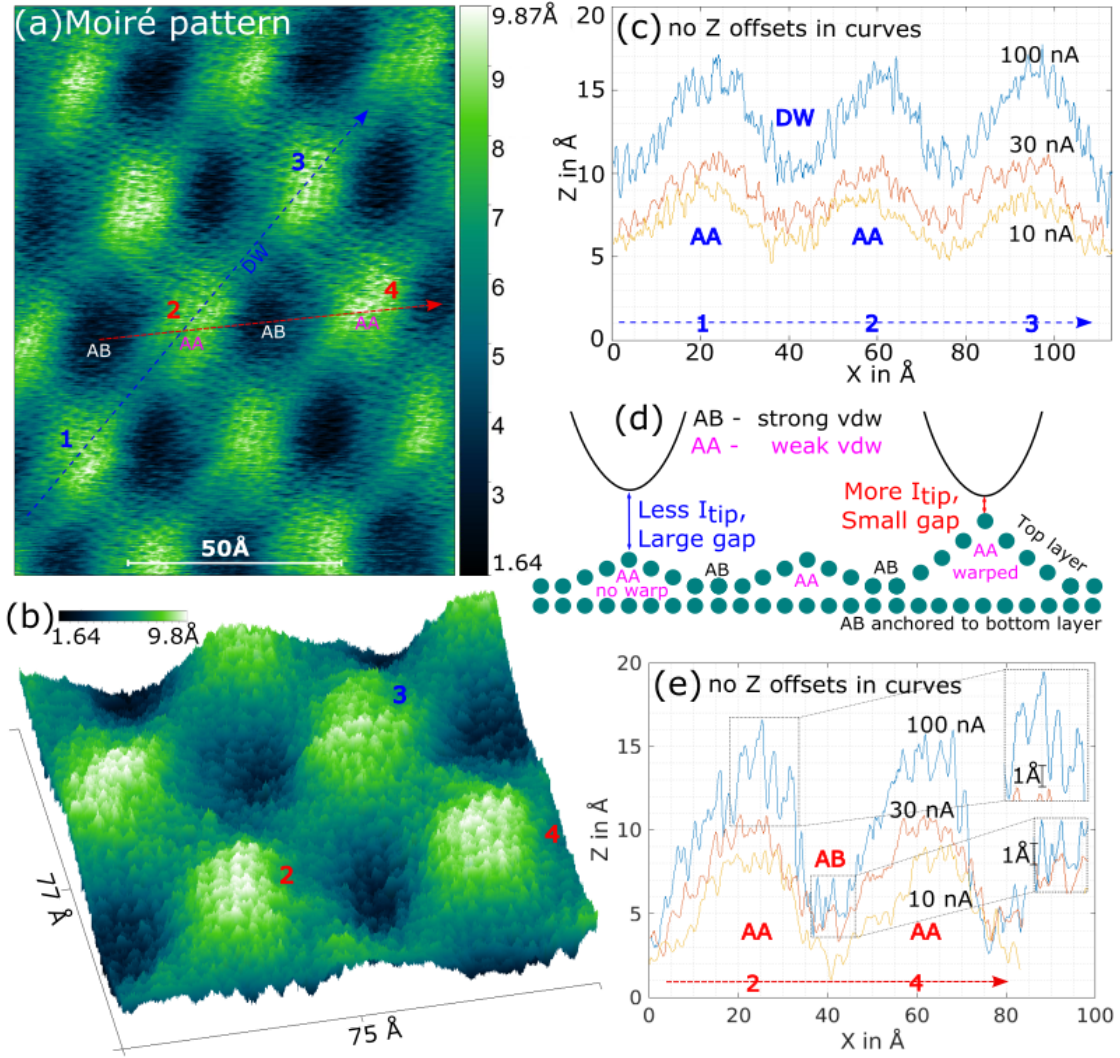


Figure 4: Probing interlayer interactions and bonding variability in Moiré pattern domains. **(a)** Two- and **(b)** Three-dimensional atomically resolved topography of Moiré pattern in graphite with a 4.2° twist angle between the top and the bottom layer. A pattern of *bright* domains (termed ‘AA’) and *dark* domains (termed ‘AB’) joined by domain walls (DW) are noted and correspond to the atomic arrangements related to the stacking configuration of the individual graphene layers. Two distinct scan directions (AA → AA → AA, along the DW: blue dotted line, and AB → AA → AB: red dotted line) are shown, with the corresponding atomic amplitude variations at differing I_{tip} in **(c)**. A high (low) atomic amplitude is observed in the AA (AB) region, due to the weak (strong) vDW-related bonding. **(d)** The contouring of the surface in the Moiré pattern is reflected in smaller (larger) tunneling currents prevalent at larger (smaller) tip-sample distance. **(e)** A scan along the AA → AB → AA direction, indicating that the AA (AB) regions are deformed outward (anchored) to the bottom layer. The inset indicates that the AA domains have higher individual atomic amplitudes compared to the AB case. The scans in **(c)** and **(e)** are not offset and consequently indicate surfaces being pulled out of plane. The DW was indicated to be of bonding strength intermediate to AA and AB regions.

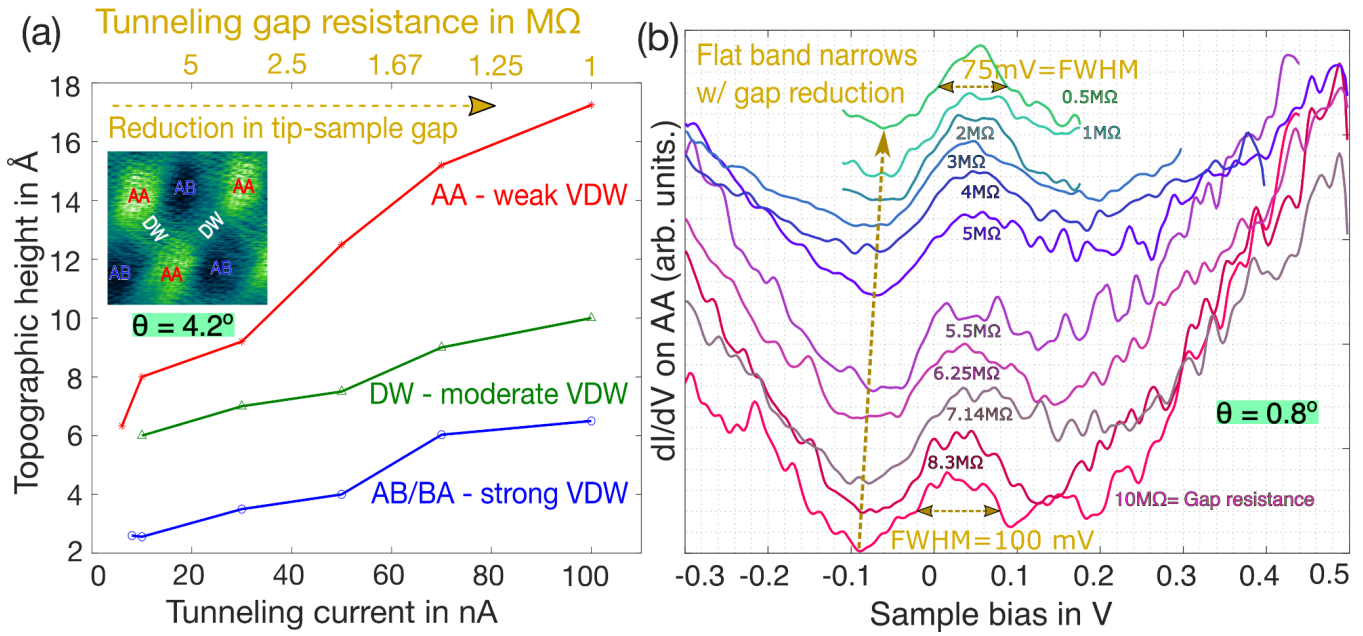


Figure 5: **Topographic and electronic response of Moiré related domains to tip-induced deformations.** (a) The measured height of the domains (AA and AB types corresponding to the graphite layer stacking) and the domain walls (DW) increases as the tip-surface gap reduces, as calibrated (?) through the variation of the tunneling current. A larger (/smaller) extent of deformation is seen for the AA (/AB) domains with an intermediate extent for the DWs. (b) Conductance (dI/dV) spectrometry on the AA domains of small twist angle ($\sim 0.8^\circ$) indicates the *onset* of flat band attributes, as deduced from the reduction of the peak full width half maxima (FWHM). Here, a reduced tip-sample gap implies greater deformation of the topmost layer and reduced independence of the layer from the bulk.

Supplementary

Supplementary Information

Atomic scale strain engineering of layered sheets on the surfaces of two-dimensional materials

N. Sarkar¹, R.C. Dynes^{2,3}, P.R. Bandaru^{2,3,4}

¹Department of Mechanical Engineering, ²Department of Physics,
³Program in Materials Science,
 University of California, San Diego, La Jolla, CA 92093-0411

S1. Atomic topography across a monatomic step between two layers

The increase in atomic amplitudes at high currents (/small gaps) are related to atomic displacements, which may then be fine-tuned though small changes in the tip current (I_{tip}). Such 'controlled' atomic deformation is one of the highlights of the present work. However, in spite of the corrugation, the step height remains constant and reaffirms the idea that the step height is a reliable calibration feature.

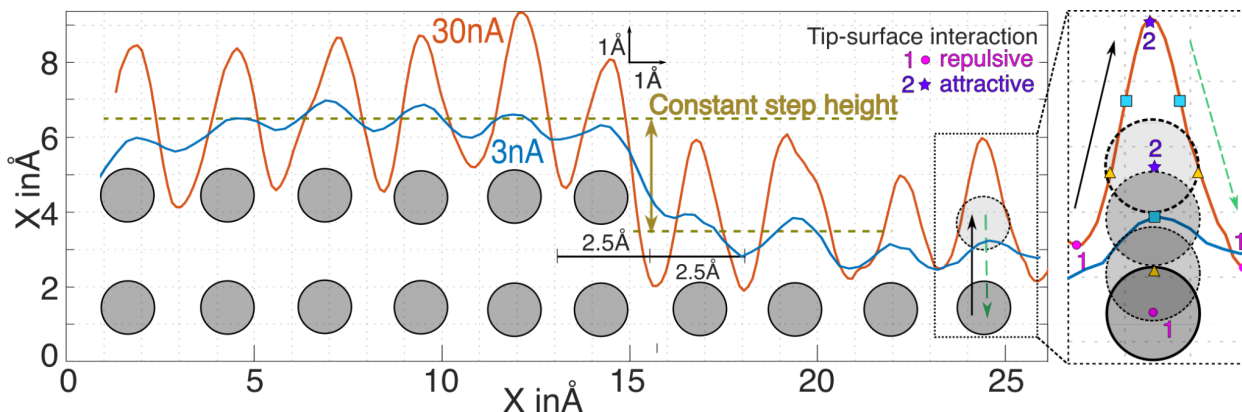


Fig. S1: Schematic atomic topography across a monatomic step between two layers.
 Comparing the topography at two different tip-sample distances, i.e., closer (/further) spacing at 30 nA (3 nA) indicates a larger (/smaller) atomic corrugation amplitude. The spatial frequency and the step height is consistent. The right inset indicates a rationale for the higher corrugations

through tip induced local deformation of an atom outwards (/inwards) related to attractive (/repulsive) tip-sample interactions and yields a guide for the indicated placement of the carbon atoms.

S2. Asymmetry in the atomic amplitude corrugations – the surface atomic layer bounded by air vis-a-vis the bulk

The extrema in the atomic topography is correlated to the atomic deformation. For instance, the local maxima (/minima) in atomic topography correspond to the outward (/inward) deformations of atoms. The deformations are asymmetrical, *i.e.* the outward (/inward) displacement invokes attractive (/repulsive) interactions due to the tip (/bulk atomic layers)[12].

Related analysis of the atomic topography, at higher tip currents/smaller gap distances, indicate relatively stable minima compared to the larger deviations in the maxima [12] Such an aspect is also evident from the fluctuations in **Fig. 1d**. It was then observed that the standard deviation (SD) of the maxima was larger than that of the minima, as a function of the I_{tip} as indicated in **Fig. S2**.

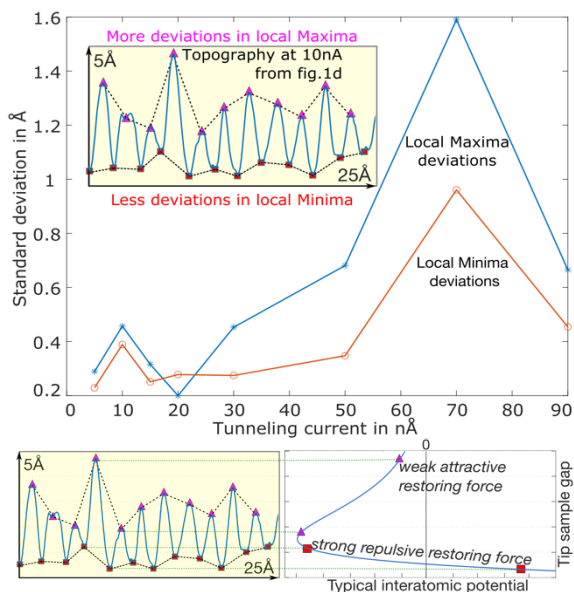


Fig. S2: Standard deviation of local maxima and minima of the atomic topography of graphite as related to **Fig.1(d)**. The bottom *inset* shows the correlation of the atomic topography to typical interatomic potential curves. The forces between the tip and the surface layer (bounded by air) exhibit strong fluctuations in contrast to the much smaller variations from the strong and constant repulsive force from the bulk.

It is then proved that the outward (/inward) deformations are indeed less (/more) restrained. Such asymmetry may also be inferred from typical interatomic potential [$V(r)$] profiles, *e.g.*, the Morse potential: $V(r) \sim \left[1 - e^{-a(r-r_o)^2}\right]$, with a as the potential profile width, r as the distance between the atoms, and r_o as the equilibrium distance, which indicate that the repulsive force is stronger than attractive force.

S3. Variation of the tunneling gap resistance (R_{gap})

In the constant current mode of the STM, an increase (/decrease) in the tip-sample gap is correlated with a decreased (/increased) I_{tip} - or increased (/decreased) V_{sample} . Such a reduction in tip-sample gap may be calibrated in terms of a reduced tunneling gap resistance: R_{gap} ($= \frac{V_{sample}}{I_{tip}}$) – indicated in **Fig. S3**

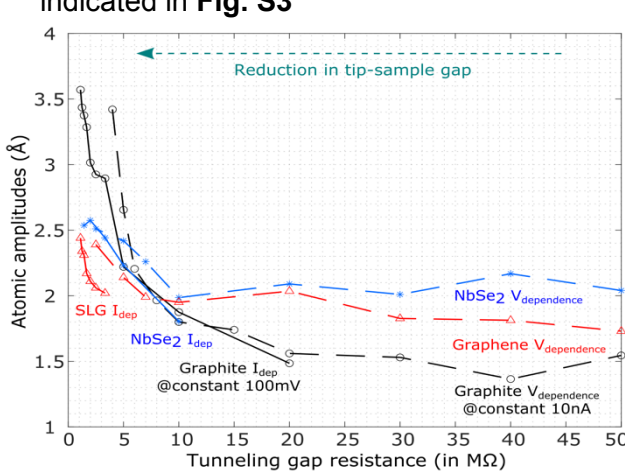


Fig. S3: Atomic amplitudes of graphite, NbSe_2 and single layer graphene (SLG) as a function of the tunneling gap resistance (R_{gap}), as estimated from **Fig. 2** – of the main text. At small (/large) gap distances, e.g., below (/above) a R_{gap} of $10 \text{ M}\Omega$, it is seen that the measured atomic amplitudes are amplified (/tend to a constant value). The atomic amplitude variations are more significant for graphite.

The coincident atomic amplitude curves of each 2D material sample generally follow an exponential variation with respect to the R_{gap} . Following an elastic model, [12] an exponential increase in the atomic amplitudes may be correlated to a linear reduction in the R_{gap} [45-47].

The onset of the enhanced atomic corrugation amplitude at R_{gap} less than $10 \text{ M}\Omega$ (also observed in Fig.1 of ref [8]) may be used as a guide to delineate the point where tip-rated deformation forces dominate the shear forces in 2D materials. It may also be indicated that R_{gap} would need to be greater than $10 \text{ M}\Omega$ to avoid any tip-induced forces disrupting STM topography measurements.

S4. The topography and spectroscopy of low angle Moiré patterns

The topography of the low twist angle (0.8°) Moiré pattern is shown in **Fig. S4**. Spectroscopic measurements were performed on AA domains (bright regions, in the figure) and results indicated in **Fig. S5**

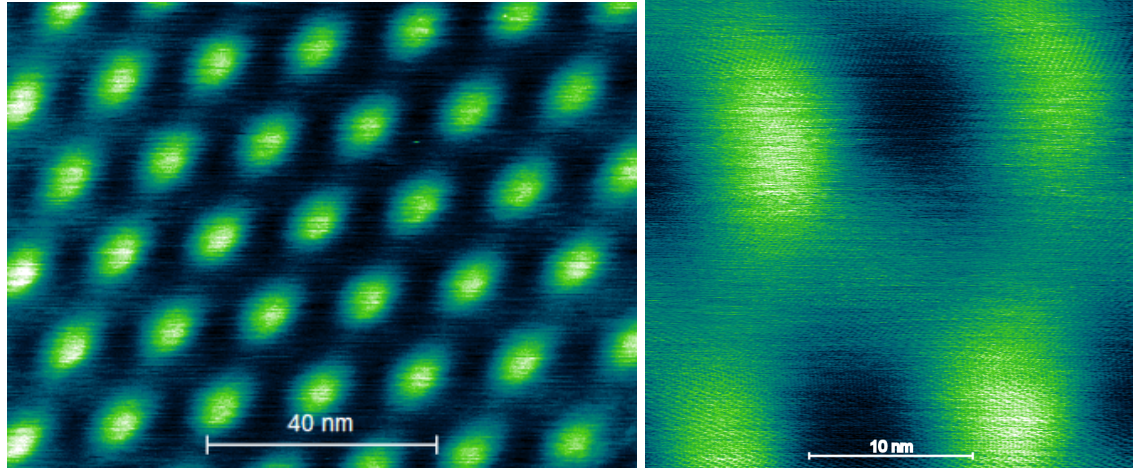


Fig. S4: The 2D topography of Moiré patterns, related to a twist angle of 0.8° .

The spectroscopy measurements utilized a lock-in modulation of 3 mV at 5 kHz. The related conductance was compared as a function of the R_{gap} in **Fig. S5 (a)**. During the measurements, the feedback loop was turned off, *i.e.*, the tip-sample gap was constant during the voltage sweeps.

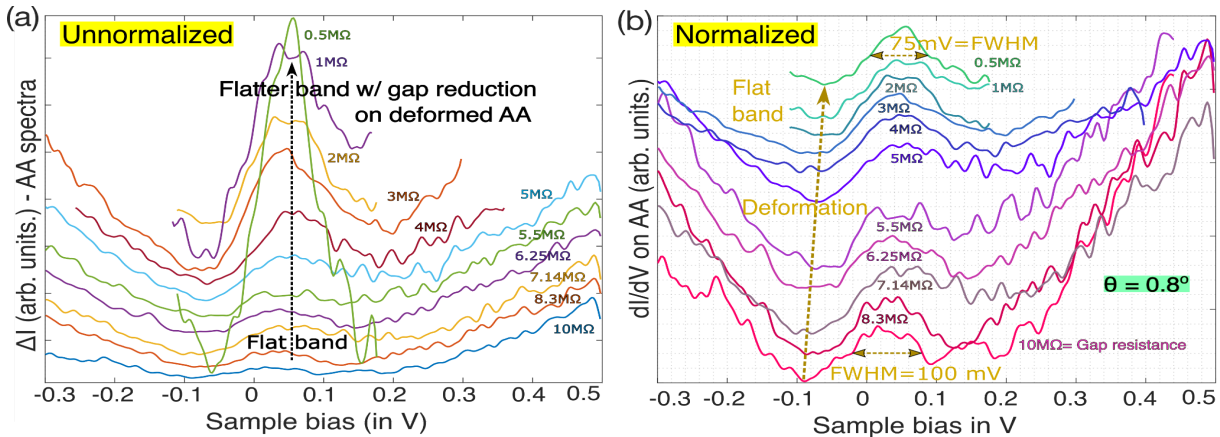


Fig. S5: Spectroscopy measurements on AA domains **(a)** unnormalized, **(b)** normalized, as a function of R_{gap} ($= \frac{V_{sample}}{I_{tip}}$). For $0.5 \text{ M}\Omega < R_{gap} < 5 \text{ M}\Omega$, the I_{tip} was fixed at 100 nA, while the V_{sample} was in the range of 50 mV to 500 mV. For $5.5 \text{ M}\Omega < R_{gap} < 10 \text{ M}\Omega$, the V_{sample} was fixed at 500 mV, while I_{tip} was varied from 50 nA to 100 nA.

The normalization is done by matching the amplitude of the zero bias peak to the same amount. Such normalization eliminates the conductance dependence with gap distance and allows to observe the changes in zero bias peak (like FWHM) as a function of deformation only.